Database of Bulk Material Properties

ET-0001A-14

D. Heinert, C. Schwarz, G. Hofmann, J. Komma, R. Nawrodt

Institut für Festkörperphysik, Friedrich-Schiller- Universität Jena

on behalf of ELiTES WP2

ET-0001A-14

Bulk thermal properties

D. Heinert, C. Schwarz, G. Hofmann, J. Komma, R. Nawrodt
on behalf of the ELiTES WP2 members

February 25, 2014

Contents

1 Introduction

Material properties play an important role in understanding thermal noise of complex systems. Future gravitational wave detectors are proposed to be operated at cryogenic temperatures. Thus, the knowledge of material properties at low temperatures is strongly required to predict their thermal noise limited sensitivity. This document describes the fundamental view of solid state physics behind relevant material properties for future gravitational wave detectors. The focus is put on potential bulk materials that will be used in these detectors - silicon and sapphire for cryogenic operation and fused silica for room temperature use. Followed by an introduction relevant physical properties are discussed for the above set of materials and summarized in form of interpolated values. A description is given how the interpolated data was obtained and under which limits it should be used. The data is also available in form of plain text files that are attached to this document.

2 Basic relations on material properties of solids

In future gravitational wave detectors mirrors and suspensions should be used at low temperatures promising a thermal noise decrease of these components. Among these detectors are KAGRA - focusing on sapphire as the cryogenic test mass material - and ET - proposing silicon test masses. For noise calculations or construction issues (e. g. the efficient extraction of absorbed laser light through the suspension fibers) detailed knowledge of the material parameters is necessary especially at the low operational temperatures.

But the properties of solids at low temperature differ significantly from everyday experience at room temperature. Without knowing the processes determining the temperature dependence of solids there is no sense in assuming properties for a low temperature operation of these materials. For that reason the main concepts to understand and predict the properties of solids at low temperatures are presented in this chapter. These concepts are a necessary ingredient to define the desired data sets on the thermal properties of sapphire, silicon and fused silica as the most interesting materials in current and future gravitational wave detectors.

2.1 Specific heat

Any object at non-zero temperature undergoes thermal motion. This is not only true for the well known special case of a Brownian particle in a fluid. In the same way also the atoms in a solid move around their equilibrium position driven by thermal energy. Consequently such a motion stores energy in the system. The following description can be found in any standard text book on solid state physics, e. g. see Ref. [1, 2]. There a more detailed view on Bose-Einstein statistics, Debye's and Einstein's model on lattice vibrations can be found.

The heat capacity C exactly describes this amount of thermal energy. To be exact it links the change of temperature T to a change in the inner energy U of the solid

$$C = \frac{dU}{dT} \ . \tag{2.1}$$

From this definition it is clear that knowing the function $U(T)$ immediately gives the solution to the desired values for the specific heat. Indeed the description using phonon statistics gives further insight into such a calculation. With the help of the density of phonon states $D(\epsilon)$ and the population density of phonons $g(\epsilon, T)$ the inner energy reads

$$U(T) = \int d\epsilon \ \epsilon \times g(\epsilon, T) \times D(\epsilon) \ , \tag{2.2}$$

with ϵ being the energy of a single phonon state. In this approach the change of the phonon dispersion and consequently of the density of states $D(\epsilon)$ with respect to temperature has been neglected. Thus temperature only affects the inner energy through the population density of phonons. As phonons are bosonic particles the Bose-Einstein statistics (see e. g. Ref. [3]) have been used for the population density

$$g(\epsilon) = \frac{1}{\exp\left(\frac{\epsilon}{k_B T}\right) - 1} \ , \tag{2.3}$$

where k_B represents Boltzmann's constant.

A detailed calculation then requires knowledge of the exact dispersion relation of the respective solid. But two approximations have been proven successful in describing the basic behavior. Using the Debye model the acoustical phonon branches are described by a linear and isotropic relation between radial frequency ω and wave number q as

$$\omega(q) = v \times q \ . \tag{2.4}$$

This behavior is adopted from the classical propagation of a sound wave with velocity v. It results in a quadratic density of states which is cut off at a maximum frequency called the Debye-frequency ω_D. Further the optical branches are approximated as delta peaks in the density of states due to a model of Einstein. At low temperatures only the acoustic branches give rise to a significant contribution to specific heat. For the case of crystals with only one element in the atomic basis it reads

$$C^a(T) \approx 3Nk_B \frac{4\pi^4}{5} \left(\frac{T}{\theta_D}\right)^3 \ . \tag{2.5}$$

Here N is the number of atoms while θ_D marks the Debye temperature and is obtained from a fit to the original phonon dispersion relation. Crystals bearing a single element in the atomic basis exhibit only acoustic branches and are fully described by Debye's model. For other crystals also the optical phonons have to be taken into account especially at high temperatures. Such an approach arrives at the Dulong-Petit law with

$$C^a(T) + C^o(T) \approx 3Nk_B \ . \tag{2.6}$$

From this number the molar heat capacity follows by dividing the heat capacity by the molar amount of the sample n via

$$c_m = \frac{C}{n} = 3R \approx 25\,\mathrm{J\,mol^{-1}\,K^{-1}} \tag{2.7}$$

For many metals the Debye temperature is well below room temperature and their specific heat at room temperature follows the prediction of Dulong and Petit. For silicon the Debye temperature is around 640 K. Thus the stationary value is not reached at room temperature. The general behavior of the molar heat capacity with respect to temperature is depicted in Fig. 2.1.

As the definition of phonons requires a periodicity in the atomic structure it becomes meaningless for amorphous solids. But also in this case a similar behavior of the specific

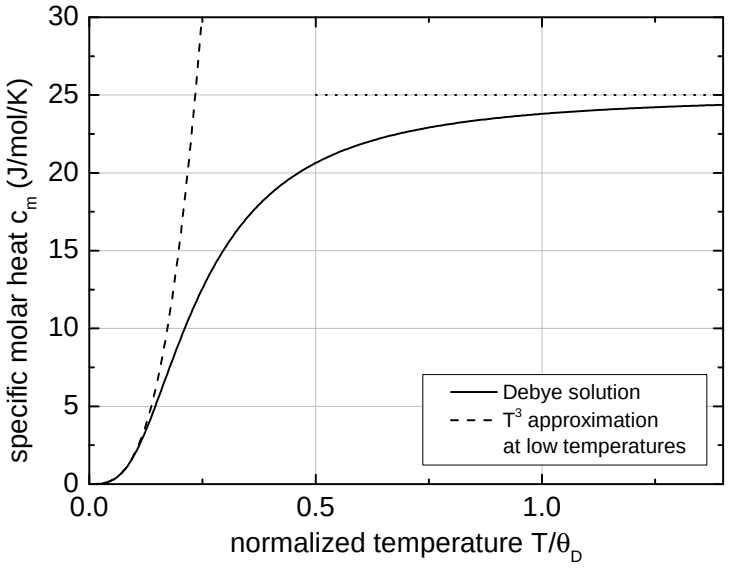

Figure 2.1: Temperature behavior of the molar specific heat predicted by Debye's theory.

heat like in crystals is observed. Here again the atoms move within their potential around the equilibrium position. At elevated temperatures each particle follows the equipartition theorem. Consequently, due to the three spatial dimensions and potential and kinetic energy each particle contributes an amount of $3k_BT$ to the inner energy of the solid.

Lowering the temperature results in the decrease of the specific heat. At low temperatures only long-wave phonons are excited. As these phonons are not able to probe the local structural disorder of an amorphous solid one is to expect that the Debye theory is still valid for amorphous solids. Nevertheless at very low temperatures (below 1 K fur amorphous silica) a deviation from the T^3 law has been measured. This deviation can be explained in terms of tunneling processes within the glassy structure (see e. g. Ref. [4]).

In principle the same treatment can be repeated to obtain the specific heat due to electrons. Here the only difference consists in replacing the Bose-Einstein distribution in Eq. 2.2 by the Fermi distribution $f(\epsilon, T)$. For metals a detailed investigation reveals an effect of

$$C^e(T) \approx D(\epsilon_F)\,\frac{\pi^2}{3}\,k_B^2 T\ , \tag{2.8}$$

for temperatures low compared to the Fermi-temperature T_F of the electrons. As T_F is in the order of 10 000 K this assumption is well fulfilled at room temperature and below. It gives a linear impact of temperature on the specific heat due to electrons. With its T^3 law the phononic contribution covers the electronic contribution at temperatures above ~ 10 K. Only at very low temperatures the electronic contribution becomes visible.

Most calculations demand for the specific heat c_p that is normalized to the mass of the material m. The connection to the heat capacity C discussed above reads

$$c_p = \frac{C}{m}\ . \tag{2.9}$$

2.2 Thermal conductivity

The parameter of thermal conductivity describes the effectiveness of a heat transport between regions of a solid exhibiting different temperatures. It is defined connecting the heat current density $\mathbf{j}$ to a temperature gradient ∇T via

$$\mathbf{j} = \kappa \nabla T \ . \tag{2.10}$$

This relation is nicely illustrated by the thermal power P transported between the two ends of a cylinder of length L and cross section A. The coefficient of thermal conductivity κ then follows from the relation

$$P = \kappa \frac{A}{L} \ , \tag{2.11}$$

showing a unit of $\mathrm{W\,m^{-1}\,K^{-1}}$.

In a simple picture of solid state physics the process of thermal conductivity can be illustrated utilizing phonons again. As a starting point for this illustration the case of two regions showing a temperature difference remains. These two regions also exhibit a different phonon population. Due to the bosonic character of phonons their number is not fixed in the system and consequently increases at higher temperatures. Looking at phonons as particles carrying an energy portion they will start to diffuse within the system. And clearly as more phonons are situated at the hot part of the sample there will be an effective flow of phonons (and thermal energy) from the hotter part to the colder part. Thus the heat flow between these two regions can be explained by the diffusion of phonons. By an analytic treatment of this process the relation

$$\kappa = \frac{1}{3} c_V v \Lambda \ , \tag{2.12}$$

can be found where c_V is specific heat per volume and v the group velocity of phonons. The free path length Λ describes the effect of phonon collisions with various crystal defects. Any structure breaking the crystalline symmetry will act as a scattering center for phonons and will decrease their free path length. Lattice defects as well as thermally moving atoms reveal the most important impact on thermal conductivity. The above equation helps explaining the typical temperature dependence of thermal conductivity in crystals. This general behavior is depicted in Fig. 2.2.

Starting at room temperature the vibrations of atoms in the crystal are quite large. This motion leads to a quite small free path length resulting in a relatively small thermal conductivity. In this regime the thermal motion is even a stronger scattering center than defects. Thus the thermal conductivity at room temperature and above is not sensitive to the defect concentrations for many materials. One nice example of this can be found for differently doped silicon samples showing nearly the same thermal conductivity at 300 K (see, e. g., Ref. [5]).

Decreasing the temperature will lead to an increase of thermal conductivity. This process is due to the reduction of thermal motion of lattice atoms and raises the path length. At intermediate temperatures (20 K to 100 K) the maximum value of thermal conductivity appears being limited by the phonon scattering on impurities. Thus a strong dependence of the maximum κ on crystal defects is experimentally observed. The above

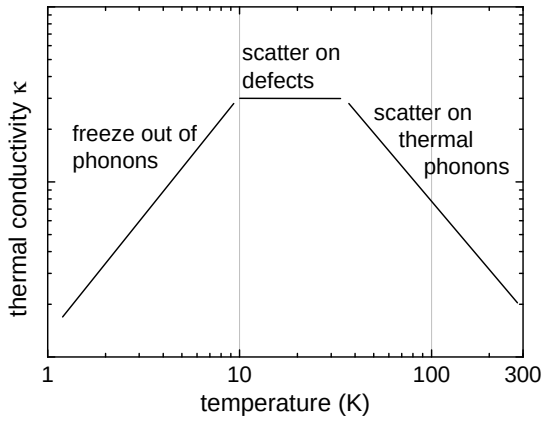

Figure 2.2: Schematic behavior of thermal conductivity in crystals. At low temperatures the freeze out of phonons as carriers for heat energy leads to a T^3 behavior. Also the phonon mean free path - and consequently κ - is limited by the geometrical dimension of the sample. Approaching higher temperatures the specific heat becomes flat and the free phonon path is limited by scatter processes with lattice defects. Finally at elevated temperatures (also at room temperature) thermal vibrations of the lattice atoms form the most important scatter centers for phonons performing the heat transport. This effect leads to a decrease of κ for increasing temperatures.

considerations are illustrated on the effect of oxygen and boron impurities in silicon in Fig. 2.3. The same mechanism explains that also an isotopic mixture of atoms in a crystal act as scatter centers and reduce the thermal conductivity. Thus very pure materials show a large increase of maximum κ for isotopically enriched samples. On an isotopically enriched silicon sample a maximum κ of $\sim 30\,000\,\mathrm{W\,m^{-1}\,K^{-1}}$ has been measured [6] indicating an increase to standard silicon by a factor of 6.

Further decreasing the temperature below 20 K does not change the phonon path length anymore. This regime is called Casimir regime and can be understood in the following manner. In general a temperature decrease will result in an increased mean free path of phonons as the thermal motion of lattice atoms is strongly suppressed. Consequently at a certain temperature Λ overcomes the dimension of the sample especially for pure samples. In this regime the phonon transport within the sample shows a ballistic behavior. Phonon scattering then only occurs at the sample surface as the most fundamental defect of any crystal. Thus the surface takes the role of the limiting scatter source at very low temperatures. The mean free path length is then replaced by the typical sample dimension and becomes constant at low temperature. In the Casimir regime a change to smaller samples promises a decrease of thermal conductivity which is also observed in experiments. An investigation of this effect is exemplarily presented in Fig. 2.4(a). Further a polishing of the surface results in an increase of the measured thermal conductivity. As the polished surface is able not only to scatter phonons but also to reflect major parts without scattering, i. e. without any change of phonon momentum, explains the experimental finding.

As in the Casimir regime the mean free phonon path remains constant it gives no temperature dependence for κ. Instead the temperature decrease lowers the number of

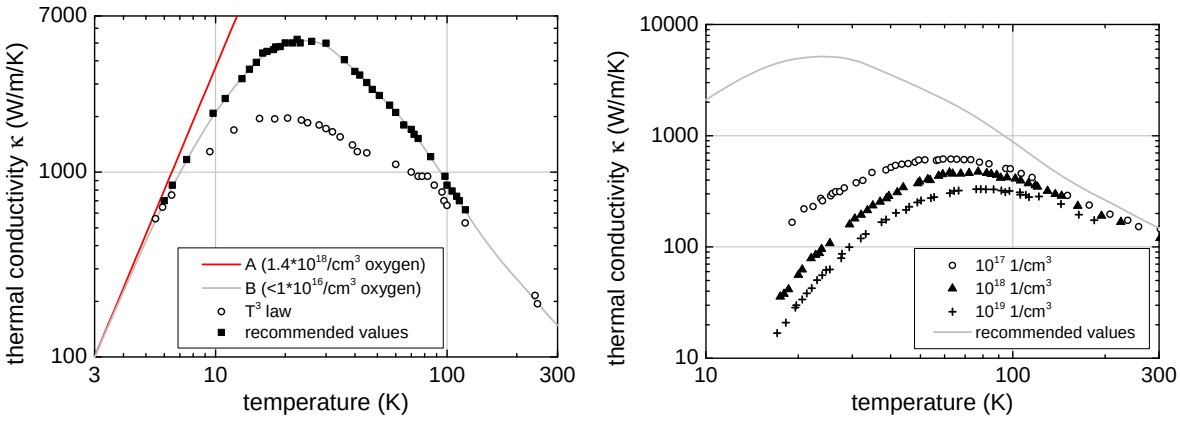

(a) Oxygen defects in silicon

(b) Boron defects in silicon

Figure 2.3: Impact of defects on the thermal conductivity of silicon. Panel (a) compares two samples with different oxygen concentrations. Data set A represents curve 21 and data set B curve 24 from Touloukian [5]. For comparison the T^3 law expected at low temperatures is inserted. Further the recommended values of thermal conductivity in silicon from Ref. [5] have been added. Panel (b) shows the effect of boron doping on thermal conductivity of silicon. Here the data of a crystalline silicon layer [7] has been used to allow the comparison between samples with identical parameters but the boron content. Due to its reduced size the layer conductivity of is below the recommended values. This maximum κ is further reduced with growing boron content. Also at low temperatures a significant decrease is visible due to the boron impurities.

excited phonons in the sample as carriers of thermal energy. This process is considered by the appearance of the specific heat in Eq. 2.12. As at low temperatures the specific heat follows a T^3 dependence (see Eq. 2.5) also κ undergoes the same strong reduction. Fig. 2.3(a) and Fig. 2.4(a) illustrate the discussed behavior.

In the whole consideration the phonon dispersion has been assumed to be independent from temperature. This assumption implies a constant group velocity v of phonons. Consequently this measure does not introduce any temperature dependence on thermal conductivity in our discussion.

In contrast to specific heat the thermal conductivity is strongly sensitive to the structural composition of the solid, i.e. for crystalline or amorphous solids. The thermal conductivity of amorphous solids is many orders of magnitude below that of crystals. This is understandable by considering amorphous solids as crystals with a large amount of defects. Consequently there will be a large number of scatter processes leading to the observed temperature dependence. A good model system for the above effect can be found in the comparison of amorphous fused silica with crystalline quartz. Both materials show the same chemical constitution but a completely different thermal conductivity as illustrated in Fig. 2.5.

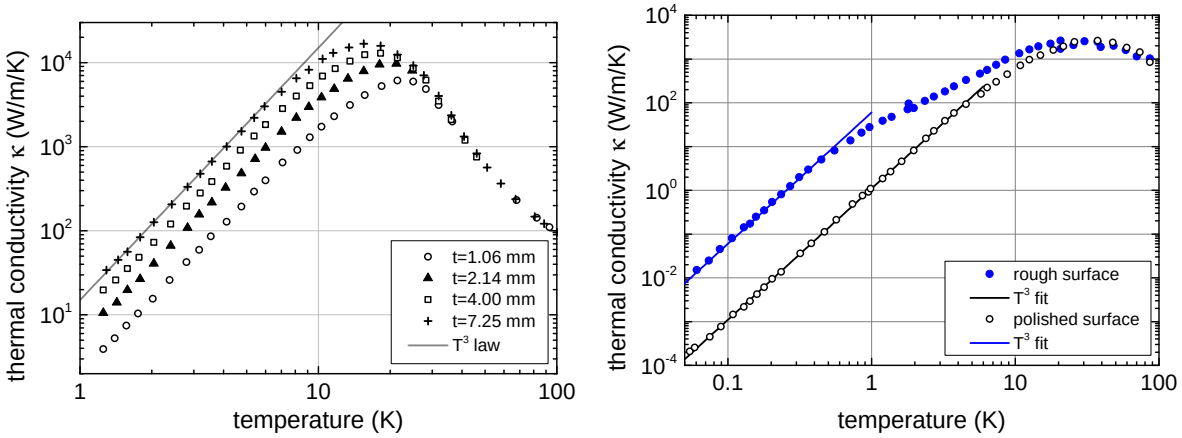

(a) LiF (b) Si

Figure 2.4: (a)Effect of sample thickness t on thermal conductivity for LiF. The data are taken from Thacher [8]. Due to Casimir's theory at low temperatures the phonon path lengths are limited by the geometry and become independent from temperature. Consequently κ follows the T^3 behavior of the specific heat at low temperatures. At high temperatures the mean free phonon path is dominated by scattering on defects and phonons, leading to the observed coincidence of the samples' thermal conductivity. (b) Effect of surface polishing on the thermal conductivity of silicon. The data are taken from Ref. [4].

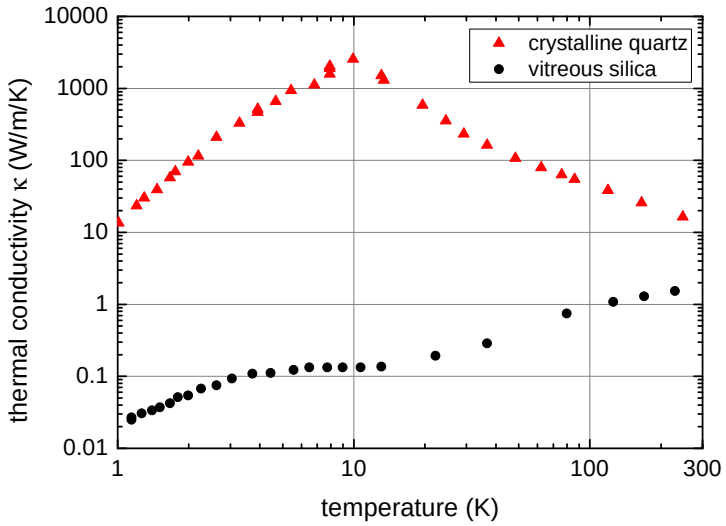

Figure 2.5: Effect of crystalline structure on the thermal conductivity in solids. Although fused silica and crystalline quartz show the same chemical constitution they show significant differences in their thermal conductivity. Especially the amorphous character of fused silica leads to a decrease of κ. Below 100 K κ of fused silica is more than two orders of magnitude below its crystalline counterpart. The presented data is taken from Zeller and Pohl [9].

2.3 Thermal expansion

In real solids a temperature change gives rise to a length change of the sample. This effect of thermal expansion is characterized by the coefficient α defined via

$$\alpha = \frac{1}{L}\frac{dL}{dT} \,, \tag{2.13}$$

where L represent the geometrical length of the sample.

In a microscopic picture thermal expansion originates from a change in the binding length of a crystal. Thus the binding potential should be investigated to explain this effect. A typical approximation can be found in the model of a harmonic potential leading to a linear force law between atoms. Such a potential exhibits equidistant energy states. Increasing the temperature excites the atom to a higher energy state leading to stronger vibrations. Due to the symmetry of the harmonic potential the mean position of the lattice atom is independent from temperature. Thus thermal expansion vanished for a purely harmonic potential.

Indeed, introducing an anharmonic contribution to the potential causes the mean binding length to depend on the energetic state of the system. Consequently a thermal length change can be observed in such system. For this reason the effect of thermal expansion is specified as an anharmonic effect. The discussed process is sketched in Fig. 2.6.

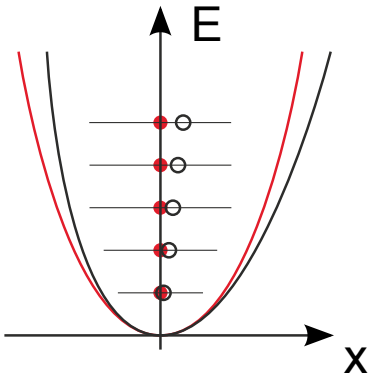

Figure 2.6: Thermal expansion as an effect of the anharmonic perturbation of the binding potential. The gray curve illustrates the pure harmonic potential. The average binding length reveals not to be energy dependent resulting in a zero thermal expansion. Adding an anharmonic contribution (black lines) changes the average position with energy. Thus a temperature change leads to an effective change of the binding length and a non-zero thermal expansion.

In solids the compressional modulus characterizes the energy necessary for a deformation, i. e. a change in binding length. Further thermal energy being independent from the crystal properties feeds the process of thermal expansion. Thus a rule of thumb can be derived connecting the existence of a high compressional modulus with a low thermal expansion and vice versa.

Finally the difference between crystalline and amorphous materials shall be discussed. As a crystal is oriented in a strongly symmetric manner any change of binding length will add to the total expansion given by the macroscopic parameter α. In contrast amorphous

materials show rotations and irregularities in their atomic constitution. Thus a change of interatomic binding length can be released within the sample. The deformation of the sample surface is reduced by this effect leading to a lower coefficient α for amorphous materials. This behavior can be illustrated by comparing fused silica and crystalline quartz again. With a mass density of $2650\,\mathrm{kg\,m^{-3}}$ crystalline quartz is denser than its amorphous counterpart showing a density of $2200\,\mathrm{kg\,m^{-3}}$. The latter fact supports the idea of the amorphous structure to be more loose and irregular compared to the crystalline one. At room temperature this manifests in $\alpha = 1.4 \times 10^{-5}\,\mathrm{K^{-1}}$ for crystalline quartz [5] and $\alpha = 3.4 \times 10^{-7}\,\mathrm{K^{-1}}$ for fused silica (Spectrosil 1400) [10].

2.4 Thermo-optic coefficient

Solids are also known to interact with electromagnetic radiation. One working mechanism consists in the formation of electric dipoles between the electrons and the lattice atoms. The incoming electromagnetic wave drives these oscillations of the electric dipoles. In turn due to their motion the dipoles emit a secondary wave depending on the electronic and lattice constitution of the crystal. In this classical oscillator model suggested by Lorentz (see Lorentz oscillator e. g. in Ref. [11]) the interaction of light with dipoles determine the refractive index of matter.

A change in the binding length is able also to change the interaction between light and matter. So via thermal expansion it is also likely to observe a temperature dependence of the refractive index. The latter is characterized by the thermo-optical parameter

$$\beta = \frac{dn}{dT} \,. \tag{2.14}$$

As the structural changes in the solid have to vanish due to the third law of thermodynamics also the coefficient β has to approach zero for low temperatures.

2.5 Elastic parameters

Under an external force any material undergoes deformations. For any point within the sample (x_1, x_2, x_3) the displacement from the unperturbed shape is represented by the vector $\mathbf{u}(x_1, x_2, x_3) = (u_x, u_y, u_z)$. Based on this quantity the strain tensor u_{ij} is defined as

$$u_{ij} = \frac{1}{2}\left(\frac{\partial u_i}{x_j} + \frac{\partial u_j}{x_i}\right) \,, \tag{2.15}$$

exhibiting a symmetry under the commutation of indices.

Further the elastic load on the material is summarized by another tensor, the stress tensor σ_{ij}. It represents the force $\vec{F}$ acting on a surface element $d\vec{S}$ of a piece of material and is defined via

$$dF_i = \sigma_{ij}\, dS_j \,, \tag{2.16}$$

where Einstein's sum convention has been used.

Then the elastic properties of a material represent the link between its deformation (in terms of strain) and the mechanical forces in the material (in terms of stress). In the leading order this relation becomes linear and is known as Hooke's law. For isotropic materials Young's modulus Y and Poisson ratio ν fully describe a solid's elastic properties leading to the relations [12]

$$u_{xx} = \frac{1}{Y}\,\sigma_{xx} - \frac{\nu}{Y}\,\left[\sigma_{yy} + \sigma_{zz}\right] \ , \tag{2.17}$$

$$u_{xy} = \frac{1+\nu}{Y}\,\sigma_{xy} \ . \tag{2.18}$$

The equations remain valid for a cyclic permutation of indices.

In the anisotropic case a tensor of fourth order is needed to link stress and strain in a material. This tensor is called stiffness tensor C_{ijkl} and results in the formulation of Hooke's law as

$$\sigma_{ij} = C_{ijkl}\,u_{kl} \ . \tag{2.19}$$

This tensor turns out to be symmetric under commutations of $i \leftrightarrow j$, $k \leftrightarrow l$ and the whole index pairs $ij \leftrightarrow kl$. If the crystal lacks any symmetry (i. e. for the triclinic class) this results in 21 independent stiffness constants. For a simple representation of a tensor of fourth order the Voigt notation is used. It relies on the contraction of index pairs following

$$11 \to 1,\ 22 \to 2,\ 33 \to 3,\ 23 \to 4,\ 13 \to 5,\ 12 \to 6 \ , \tag{2.20}$$

allowing the tranformation to a two-dimensional matrix. For the triclinic case the Voigt notation of the stiffness tensor reads

$$\hat{C}_{ij} = \begin{pmatrix} c_{11} & c_{12} & c_{13} & c_{14} & c_{15} & c_{16} \\ & c_{22} & c_{23} & c_{24} & c_{25} & c_{26} \\ & & c_{33} & c_{34} & c_{35} & c_{36} \\ & & & c_{44} & c_{45} & c_{46} \\ & & & & c_{55} & c_{56} \\ & & & & & c_{66} \end{pmatrix} \ . \tag{2.21}$$

As the matrix is symmetric only the upper half of its components is presented.

Additional symmetries of the crystal lead to the reduction of independent coefficients and to a simplification of the above structure. The resulting form of the stiffness tensor can be found in standard text books of the subject, e. g. in [13]. In the most symmetric case of an isotropic body one finds a stiffness matrix of

$$\hat{C}^{(iso)}_{ij} = \begin{pmatrix} c_{11} & c_{12} & c_{12} & 0 & 0 & 0 \\ & c_{11} & c_{12} & 0 & 0 & 0 \\ & & c_{11} & 0 & 0 & 0 \\ & & & c_{44} & 0 & 0 \\ & & & & c_{44} & 0 \\ & & & & & c_{44} \end{pmatrix} \ . \tag{2.22}$$

The relation to the parameters discussed above (Y, ν) is given by the relations

$$c_{11} = \frac{(1-\nu)Y}{(1+\nu)(1-2\nu)} \ , \ c_{12} = \frac{\nu Y}{(1+\nu)(1-2\nu)} \ , \ c_{44} = \frac{Y}{1+\nu} \ . \tag{2.23}$$

Sometimes it is useful to adopt the tensor components to a change of the coordinate system. This represents one possibility to account for different crystal orientation in any mechanical analysis. Any linear coordinate transform (unit vectors $\mathbf{e}_i \rightarrow \mathbf{e}'_i$) can be described by a matrix A_{ij}. Then the components in the new basis x'_i follow from

$$x'_i = A_{ij} x_j \ , \tag{2.24}$$

where the components in the old basis are given by x_j. In a similar way the elasticity tensor (being of fourth rank) transforms under the same basis change following

$$C'_{ijkl} = A_{i\,\hat{i}} A_{j\,\hat{j}} A_{k\,\hat{k}} A_{l\,\hat{l}} \times C_{\hat{i}\hat{j}\hat{k}\hat{l}} \ . \tag{2.25}$$

Note that this transformation law is only valid in the four dimensional treatment of the elasticity tensor. It does not hold under the two-dimensional simplification in terms of the Voigt notation.

In a finite element approach (using COMSOL [14]) there are even simpler methods to allow for a crystalline reorientation. One is to rotate the geometry in the global coordinate system. A second possibility is to rotate the material coordinate system with respect to the global coordinate system.

3 Data sets of thermal properties for selected materials

3.1 Fused Silica

3.1.1 Elastic properties

Due to its amorphous structure fused silica exhibits an isotropic behavior also in terms of elasticity. It is thus characterized by the parameters of Young's modulus Y and Poisson ratio ν. Following McSkimin [15] their value at 20 °C read

$$Y = 72.9\,\mathrm{GPa}\ ,\ \text{and}\ \nu = 0.155\ . \tag{3.1}$$

In contrast to silicon or sapphire a decrease of Young's modulus is observed heading to lower temperatures. As the typical change from 20 °C down to −200 °C is below 5% [15] it can be neglected in most calculations. A typical density for fused silica is taken from Ref. [15] as $\rho = 2203\,\mathrm{kg\,m^{-3}}$.

3.1.2 Thermal properties

Thermal expansion

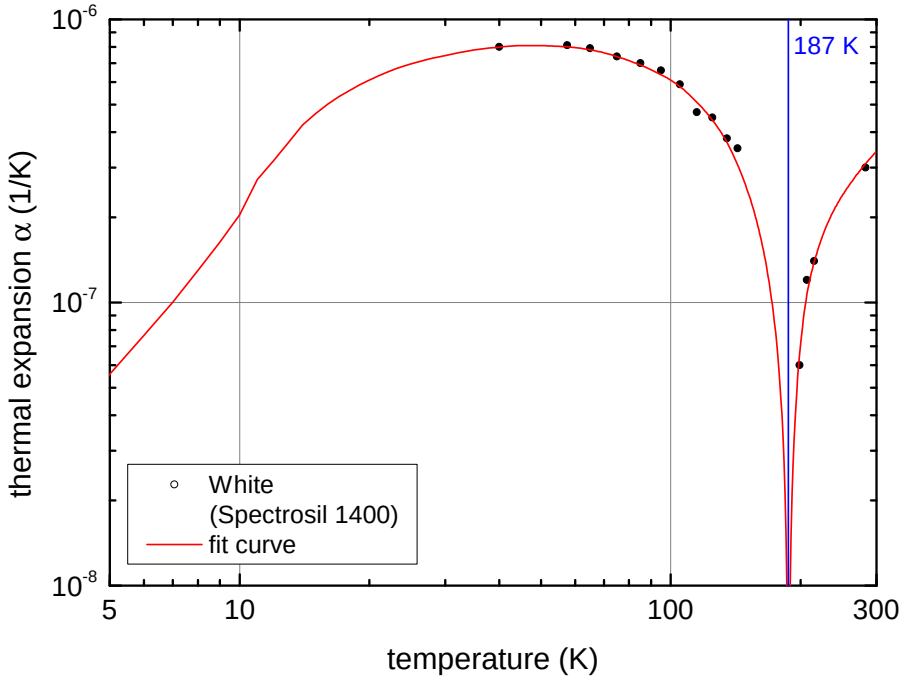

Experimental values have been taken from measurements on Spectrosil 1400 by White [10]. Note that α is negative below 187 K.

Thermo-optic coefficient

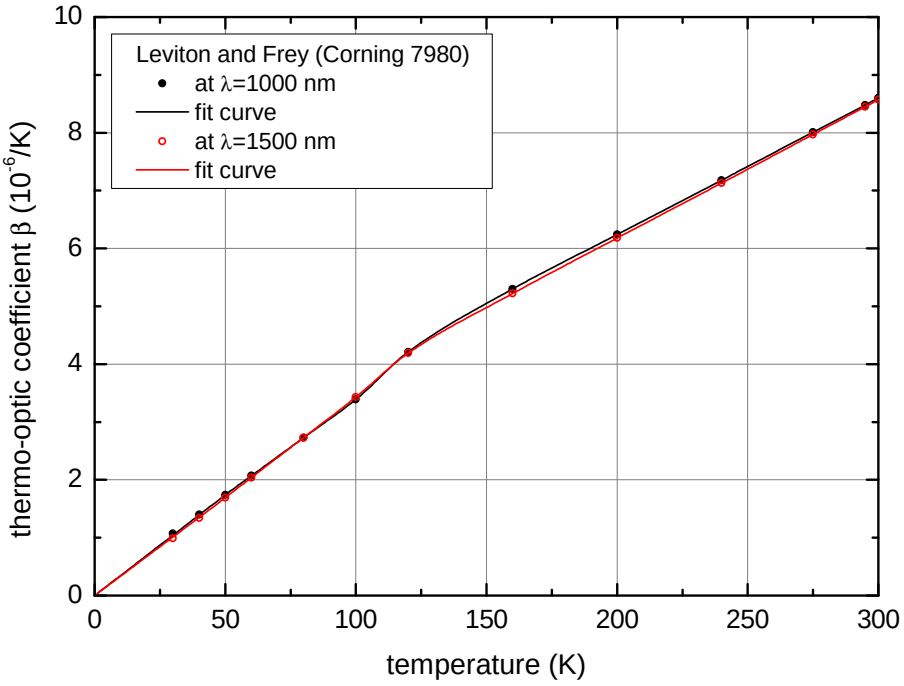

Experimental values have been taken from measurements on Corning 7980 by Leviton and Frey [16].

Specific heat

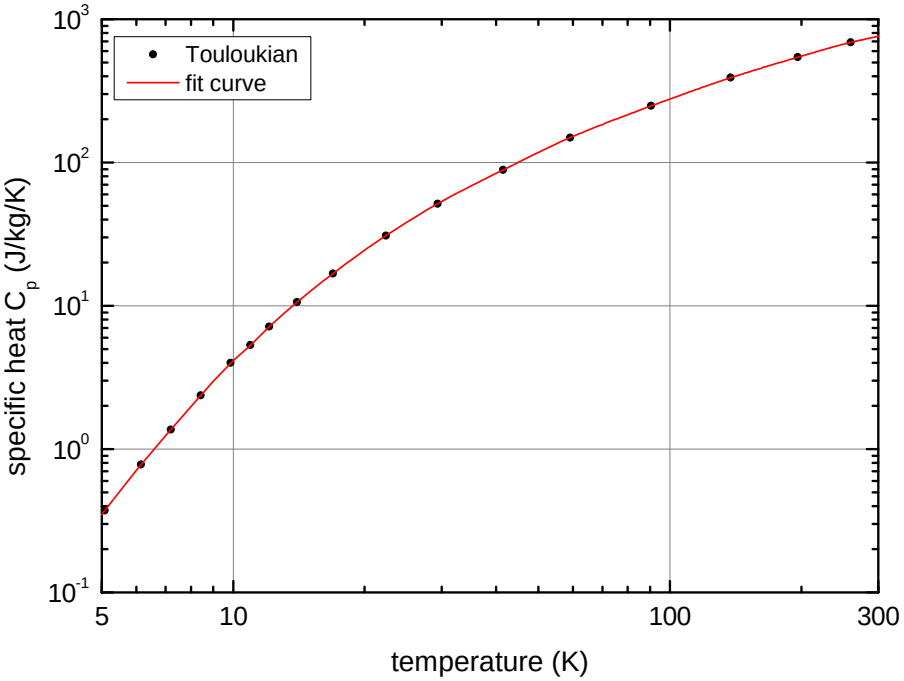

Experimental values have been taken from Touloukian [5].

Thermal conductivity

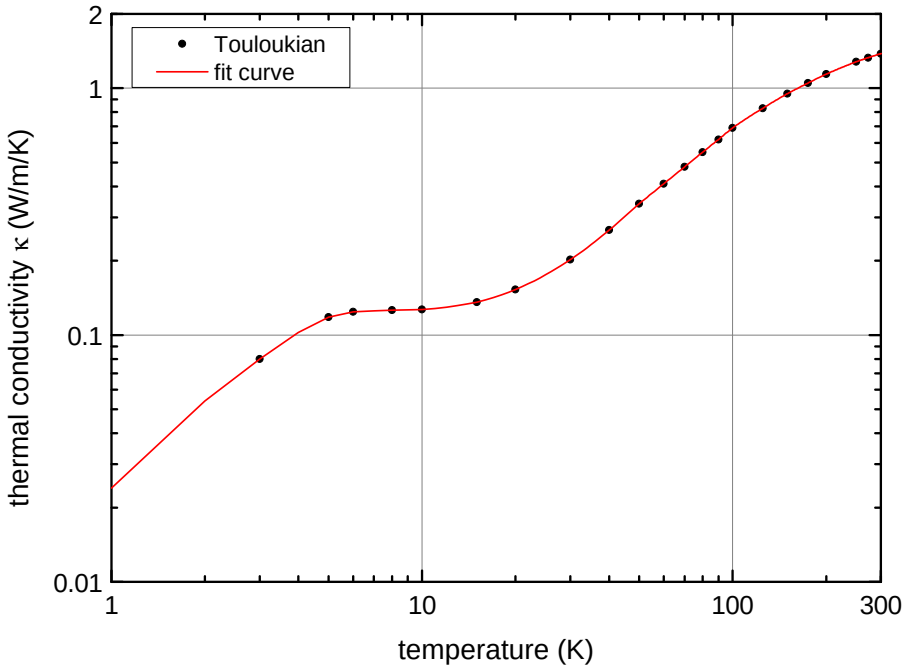

Experimental values have been taken from Touloukian [5].

Data set

An excerpt of the numerical data is given in the following table. Extrapolations in the low temperature regime have been performed assuming a T^3 law. Only for β a linear relation has been used.

T (K)	α (K^{-1})	β (K^{-1}) at λ=1500 nm	β (K^{-1}) at λ=1000 nm	C_p ($J\,kg^{-1}\,K^{-1}$)	κ ($W\,m^{-1}\,K^{-1}$)
1	-3.38×10^{-9}	3.38×10^{-8}	3.48×10^{-8}	1.86×10^{-3}	2.40×10^{-2}
2	-1.28×10^{-8}	6.75×10^{-8}	6.96×10^{-8}	1.49×10^{-2}	5.40×10^{-2}
3	-2.48×10^{-8}	1.01×10^{-7}	1.04×10^{-7}	5.35×10^{-2}	8.00×10^{-2}
4	-3.87×10^{-8}	1.35×10^{-7}	1.39×10^{-7}	1.58×10^{-1}	1.02×10^{-1}
5	-5.59×10^{-8}	1.69×10^{-7}	1.74×10^{-7}	3.51×10^{-1}	1.18×10^{-1}
6	-7.67×10^{-8}	2.03×10^{-7}	2.09×10^{-7}	7.11×10^{-1}	1.24×10^{-1}
7	-1.00×10^{-7}	2.36×10^{-7}	2.44×10^{-7}	1.24	1.25×10^{-1}
8	-1.30×10^{-7}	2.70×10^{-7}	2.78×10^{-7}	1.98	1.26×10^{-1}
9	-1.64×10^{-7}	3.04×10^{-7}	3.13×10^{-7}	2.97	1.27×10^{-1}
10	-2.04×10^{-7}	3.38×10^{-7}	3.48×10^{-7}	4.16	1.27×10^{-1}
12	-3.18×10^{-7}	4.05×10^{-7}	4.18×10^{-7}	7.01	1.30×10^{-1}
14	-4.25×10^{-7}	4.73×10^{-7}	4.87×10^{-7}	1.06×10^{1}	1.34×10^{-1}
16	-5.01×10^{-7}	5.40×10^{-7}	5.57×10^{-7}	1.47×10^{1}	1.39×10^{-1}
18	-5.62×10^{-7}	6.08×10^{-7}	6.26×10^{-7}	1.94×10^{1}	1.45×10^{-1}
20	-6.11×10^{-7}	6.75×10^{-7}	6.96×10^{-7}	2.45×10^{1}	1.53×10^{-1}
22	-6.52×10^{-7}	7.43×10^{-7}	7.66×10^{-7}	2.99×10^{1}	1.61×10^{-1}

T (K)	α (K^{-1})	β (K^{-1}) at λ=1500 nm	β (K^{-1}) at λ=1000 nm	C_p ($J\,kg^{-1}\,K^{-1}$)	κ ($W\,m^{-1}\,K^{-1}$)
24	-6.84×10^{-7}	8.10×10^{-7}	8.35×10^{-7}	3.55×10^{1}	1.71×10^{-1}
26	-7.09×10^{-7}	8.78×10^{-7}	9.05×10^{-7}	4.14×10^{1}	1.81×10^{-1}
28	-7.29×10^{-7}	9.45×10^{-7}	9.74×10^{-7}	4.74×10^{1}	1.91×10^{-1}
30	-7.46×10^{-7}	1.01×10^{-6}	1.04×10^{-6}	5.35×10^{1}	2.02×10^{-1}
32	-7.61×10^{-7}	1.08×10^{-6}	1.11×10^{-6}	5.95×10^{1}	2.14×10^{-1}
34	-7.74×10^{-7}	1.15×10^{-6}	1.18×10^{-6}	6.55×10^{1}	2.26×10^{-1}
36	-7.85×10^{-7}	1.22×10^{-6}	1.25×10^{-6}	7.16×10^{1}	2.39×10^{-1}
38	-7.92×10^{-7}	1.28×10^{-6}	1.32×10^{-6}	7.77×10^{1}	2.52×10^{-1}
40	-7.98×10^{-7}	1.35×10^{-6}	1.39×10^{-6}	8.40×10^{1}	2.66×10^{-1}
45	-8.08×10^{-7}	1.52×10^{-6}	1.57×10^{-6}	1.00×10^{2}	3.03×10^{-1}
50	-8.08×10^{-7}	1.69×10^{-6}	1.74×10^{-6}	1.18×10^{2}	3.40×10^{-1}
55	-8.04×10^{-7}	1.87×10^{-6}	1.91×10^{-6}	1.35×10^{2}	3.75×10^{-1}
60	-7.96×10^{-7}	2.04×10^{-6}	2.07×10^{-6}	1.52×10^{2}	4.10×10^{-1}
65	-7.81×10^{-7}	2.21×10^{-6}	2.24×10^{-6}	1.68×10^{2}	4.45×10^{-1}
70	-7.63×10^{-7}	2.39×10^{-6}	2.40×10^{-6}	1.84×10^{2}	4.80×10^{-1}
75	-7.39×10^{-7}	2.56×10^{-6}	2.57×10^{-6}	2.00×10^{2}	5.15×10^{-1}
80	-7.15×10^{-7}	2.73×10^{-6}	2.73×10^{-6}	2.16×10^{2}	5.50×10^{-1}
85	-6.90×10^{-7}	2.90×10^{-6}	2.89×10^{-6}	2.31×10^{2}	5.85×10^{-1}
90	-6.64×10^{-7}	3.08×10^{-6}	3.05×10^{-6}	2.47×10^{2}	6.20×10^{-1}
95	-6.38×10^{-7}	3.25×10^{-6}	3.22×10^{-6}	2.62×10^{2}	6.56×10^{-1}
100	-6.10×10^{-7}	3.43×10^{-6}	3.39×10^{-6}	2.78×10^{2}	6.90×10^{-1}
110	-5.45×10^{-7}	3.82×10^{-6}	3.81×10^{-6}	3.08×10^{2}	7.50×10^{-1}
120	-4.75×10^{-7}	4.19×10^{-6}	4.21×10^{-6}	3.39×10^{2}	8.04×10^{-1}
130	-4.05×10^{-7}	4.48×10^{-6}	4.52×10^{-6}	3.68×10^{2}	8.56×10^{-1}
140	-3.29×10^{-7}	4.74×10^{-6}	4.80×10^{-6}	3.97×10^{2}	9.05×10^{-1}
150	-2.53×10^{-7}	4.98×10^{-6}	5.05×10^{-6}	4.24×10^{2}	9.50×10^{-1}
160	-1.81×10^{-7}	5.22×10^{-6}	5.30×10^{-6}	4.51×10^{2}	9.92×10^{-1}
170	-1.12×10^{-7}	5.47×10^{-6}	5.55×10^{-6}	4.77×10^{2}	1.03
180	-4.62×10^{-8}	5.71×10^{-6}	5.78×10^{-6}	5.03×10^{2}	1.07
190	1.48×10^{-8}	5.94×10^{-6}	6.01×10^{-6}	5.28×10^{2}	1.11
200	7.14×10^{-8}	6.18×10^{-6}	6.24×10^{-6}	5.52×10^{2}	1.14
210	1.20×10^{-7}	6.42×10^{-6}	6.48×10^{-6}	5.77×10^{2}	1.17
220	1.56×10^{-7}	6.66×10^{-6}	6.71×10^{-6}	6.02×10^{2}	1.20
230	1.87×10^{-7}	6.89×10^{-6}	6.94×10^{-6}	6.26×10^{2}	1.23
240	2.15×10^{-7}	7.13×10^{-6}	7.18×10^{-6}	6.49×10^{2}	1.26
250	2.39×10^{-7}	7.37×10^{-6}	7.42×10^{-6}	6.71×10^{2}	1.28
260	2.61×10^{-7}	7.61×10^{-6}	7.65×10^{-6}	6.90×10^{2}	1.30
270	2.83×10^{-7}	7.85×10^{-6}	7.89×10^{-6}	7.09×10^{2}	1.32
280	3.04×10^{-7}	8.09×10^{-6}	8.13×10^{-6}	7.27×10^{2}	1.34
290	3.23×10^{-7}	8.33×10^{-6}	8.36×10^{-6}	7.44×10^{2}	1.36
300	3.43×10^{-7}	8.57×10^{-6}	8.60×10^{-6}	7.61×10^{2}	1.38

3.2 Sapphire

3.2.1 Lattice structure

In the following the lattice properties of sapphire have been taken from Ref. [17]. Sapphire condensates in a trigonal crystal system belonging to the point group D_{3d}. Thus its unit cell can be described with a rhombohedral basis given by

$$\mathbf{a}_1 = \left(\frac{\sqrt{3}}{2}s, -\frac{s}{2}, r\right) \ , \ \mathbf{a}_2 = (0, s, r) \ , \ \mathbf{a}_3 = \left(-\frac{\sqrt{3}}{2}s, -\frac{s}{2}, r\right) \ . \tag{3.2}$$

Here the x-axis is oriented along a twofold axis of the crystal and s and r represent the lattice constants. They are transformed to the more usual constants of a hexagonal system via

$$3r = c_H = 12.99\,\text{Å} \ , \ \sqrt{3}s = a_H = 4.76\,\text{Å} \ . \tag{3.3}$$

The rhombohedral unit cell shows a total of 4 Al and 6 O atoms as the atomic basis of one unit cell. It can be transformed into a hexagonal unit cell by the following modification

$$\mathbf{a}_1 - \mathbf{a}_2 = \quad \sqrt{3}s\left(\frac{1}{2}, -\frac{\sqrt{3}}{2}, 0\right) = \quad a_H\left(\frac{1}{2}, -\frac{\sqrt{3}}{2}, 0\right) = \quad \mathbf{A}_1 \ , \tag{3.4}$$

$$\mathbf{a}_2 - \mathbf{a}_3 = \quad \sqrt{3}s\left(\frac{1}{2}, \frac{\sqrt{3}}{2}, 0\right) = \quad a_H\left(\frac{1}{2}, \frac{\sqrt{3}}{2}, 0\right) = \quad \mathbf{A}_2 \ , \tag{3.5}$$

$$\mathbf{a}_1 + \mathbf{a}_2 + \mathbf{a}_3 = \quad (0, 0, 3r) = \quad c_H(0, 0, 1) = \quad \mathbf{A}_3 \ . \tag{3.6}$$

The basis vectors $\mathbf{A}_i$ represent a hexahedral lattice with the usual lattice constants a_H and c_H. The benefit of a simpler lattice structure is accompanied by an increased unit cell volume leading to an atomic basis consisting of 30 atoms instead of 10 for the rhombohedral unit cell.

The growth of large sapphire crystals is restricted to three major orientations [18]: $\{10\bar{1}0\}$ (M-plane), $\{11\bar{2}0\}$ (A-plane) and $\{1\bar{1}02\}$ (R-plane). Here the four-index scheme of labeling crystal planes has been used as lattice symmetries are easier to be identified within this system. In this notation indexing a lattice plane by $(hkil)$ represents a plane with the classical miller indeces of (hkl) while the index i is redundant and only inserted to realize symmetries. It follows the relation $i = -h - k$. To illustrate the orientation of the above planes it is helpful to present their normal vector in real space. For this purpose the reciprocal lattice vectors of $\mathbf{A}_i$ have to be calculated using the relation

$$\mathbf{B}_1 = \frac{2\pi}{\Omega_0}(\mathbf{A}_2 \times \mathbf{A}_3) \ , \ \Omega_0 \equiv \mathbf{A}_1 \cdot (\mathbf{A}_2 \times \mathbf{A}_3) \ , \tag{3.7}$$

and its cyclic permutations. Ω_0 represents the volume of the hexagonal unit cell. This calculation reveals

$$\mathbf{B}_1 = \frac{4\pi}{\sqrt{3}a_H}\left(\frac{\sqrt{3}}{2}, -\frac{1}{2}, 0\right) \ , \ \mathbf{B}_2 = \frac{4\pi}{\sqrt{3}a_H}\left(\frac{\sqrt{3}}{2}, \frac{1}{2}, 0\right) \ , \ \mathbf{B}_3 = \frac{2\pi}{c_H}(0, 0, 1) \ . \tag{3.8}$$

Knowing the inverse lattice vectors allows to calculate the surface normals in real space revealing the results given in Tab. 3.2. A visualization of the planes is given in Fig. 3.1.

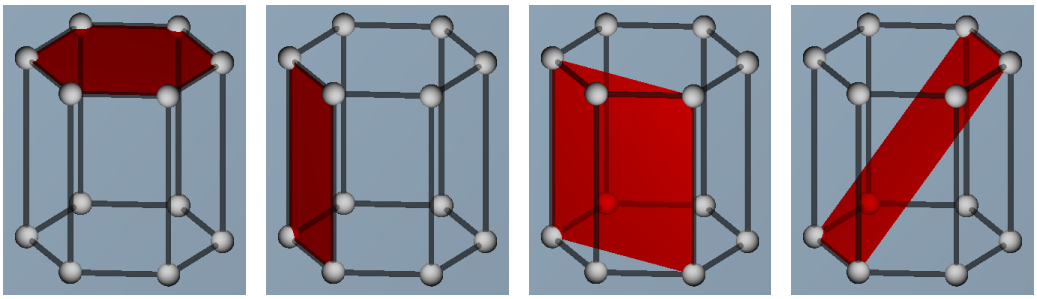

(a) C-plane (b) M-plane (c) A-plane (d) R-plane

Figure 3.1: Visualization of the major growing planes in sapphire. The 3-fold axis is along the normal to the hexagonal area while the 2-fold axes are along the lines between the center of the hexagonal area to one lattice point.

3.2.2 Elastic properties

The point group of sapphire D_{3d} allows the appearence of six independent elastic constants. In the Voigt notation the elastic stiffness tensor reads

$$\hat{C}_{ij} = \begin{pmatrix} c_{11} & c_{12} & c_{13} & c_{14} & 0 & 0 \\ & c_{11} & c_{13} & -c_{14} & 0 & 0 \\ & & c_{33} & 0 & 0 & 0 \\ & & & c_{44} & 0 & 0 \\ & & & & c_{44} & c_{14} \\ & & & & & c_{66} \end{pmatrix} , \tag{3.9}$$

where the component c_{66} follows the relation

$$c_{66} = \frac{1}{2}\left(c_{11} - c_{12}\right) \ . \tag{3.10}$$

The elastic constants at room temperature as well as their behavior at lower temperatures have been measured by Tefft [19]. In his work Tefft measured the elastic constants down to 80 K and extrapolated his results down to 0 K. Due to this extrapolation the relative change in each elastic component turns out to be below 3% being negligibly small for most practical calculations. The measured elastic constants at 27 °C are taken from [20]

Table 3.2: Normal vectors of characteristic growth directions of sapphire in real space. The normal vectors are presented in cartesian coordinates.

plane	normal vector $\mathbf{n}$	comments
C-plane (0001)	$\mathbf{B}_3 \propto (0,0,1)$	3-fold axis
M-plane $(10\bar{1}0)$	$\mathbf{B}_1 \propto (\sqrt{3}/2, -1/2, 0)$	bisectrix of two 2-fold axes
A-plane $(11\bar{2}0)$	$\mathbf{B}_1 + \mathbf{B}_2 \propto (1,0,0)$	2-fold axis
R-plane $(1\bar{1}02)$	$\mathbf{B}_1 - \mathbf{B}_2 + 2\mathbf{B}_3 \propto (0, -1/\sqrt{3}, a_H/c_H)$	

and read

$$c_{11} = 490.2\,\mathrm{GPa}, \qquad c_{12} = 165.4\,\mathrm{GPa}, \qquad c_{33} = 490.2\,\mathrm{GPa}, \tag{3.11}$$

$$c_{13} = 113.0\,\mathrm{GPa}, \qquad c_{14} = -23.2\,\mathrm{GPa}, \qquad c_{44} = 145.4\,\mathrm{GPa}, \tag{3.12}$$

$$\Rightarrow c_{66} = 162.4\,\mathrm{GPa}\ . \tag{3.13}$$

A typical density of sapphire reads

$$\rho = 3980\,\mathrm{kg\,m^{-3}}\ . \tag{3.14}$$

In noise calculations the anisotropic character of sapphire has to be considered. With this respect typical finite element codes allow to orient the geometry axis within the coordinates of the elastic tensor. The other way presented here is to transform the elastic tensor to new coordinates and present the new component values of this tensor. Table 3.3 illustrates the results of this process.

Table 3.3: Elasticity tensor for sapphire along different crystallographic axes. The Voigt notation $\hat{C}_{ij}$ is used to show the components of the elasticity tensor. In the presented coordinates the z axis is oriented along the growing direction. All presented values are valid for a temperature of 27 °C and taken from [20].

orientation	A_{ij}	$\hat{C}_{ij}$
A-cut	$\begin{pmatrix} 0 & 0 & -1 \\ 0 & 1 & 0 \\ 1 & 0 & 0 \end{pmatrix}$	$\begin{pmatrix} c_{33} & c_{13} & c_{13} & 0 & 0 & 0 \\ & c_{11} & c_{12} & 0 & 0 & c_{14} \\ & & c_{11} & 0 & 0 & -c_{14} \\ & & & c_{66} & -c_{14} & 0 \\ & & & & c_{44} & 0 \\ & & & & & c_{44} \end{pmatrix}$
M-cut	$\begin{pmatrix} 0 & 0 & -1 \\ \frac{1}{2} & \frac{\sqrt{3}}{2} & 0 \\ \frac{\sqrt{3}}{2} & -\frac{1}{2} & 0 \end{pmatrix}$	$\begin{pmatrix} c_{33} & c_{13} & c_{13} & 0 & 0 & 0 \\ & c_{11} & c_{12} & 0 & -c_{14} & 0 \\ & & c_{11} & 0 & c_{14} & 0 \\ & & & c_{66} & 0 & -c_{14} \\ & & & & c_{44} & 0 \\ & & & & & c_{44} \end{pmatrix}$
$c_{11} = 490.2\,\text{GPa}$, $c_{12} = 165.4\,\text{GPa}$, $c_{33} = 490.2\,\text{GPa}$, $c_{13} = 113.0\,\text{GPa}$, $c_{14} = -23.2\,\text{GPa}$, $c_{44} = 145.4\,\text{GPa}$, $c_{66} = 162.4\,\text{GPa}$.		
R-cut	$\begin{pmatrix} 1 & 0 & 0 \\ 0 & \frac{\sqrt{3}\chi}{\sqrt{3\chi^2+1}} & -\frac{1}{\sqrt{3\chi^2+1}} \\ 0 & \frac{1}{\sqrt{3\chi^2+1}} & \frac{\sqrt{3}\chi}{\sqrt{3\chi^2+1}} \end{pmatrix}$ $\chi \equiv a_H/c_H$	$\begin{pmatrix} e_{11} & e_{12} & e_{13} & e_{14} & 0 & 0 \\ & e_{22} & e_{23} & e_{24} & 0 & 0 \\ & & e_{33} & e_{34} & 0 & 0 \\ & & & e_{44} & 0 & 0 \\ & & & & e_{55} & e_{56} \\ & & & & & e_{66} \end{pmatrix}$
$e_{11} = 490.2\,\text{GPa}$, $e_{22} = 466.9\,\text{GPa}$, $e_{33} = 424.9\,\text{GPa}$, $e_{12} = 107.0\,\text{GPa}$, $e_{13} = 171.4\,\text{GPa}$, $e_{23} = 157.3\,\text{GPa}$, $e_{44} = 189.7\,\text{GPa}$, $e_{55} = 178.5\,\text{GPa}$, $e_{66} = 129.3\,\text{GPa}$, $e_{14} = -13.8\,\text{GPa}$, $e_{24} = 4.3\,\text{GPa}$, $e_{34} = -14.2\,\text{GPa}$, $e_{56} = 2.2\,\text{GPa}$.		

3.2.3 Thermal properties

Thermal expansion

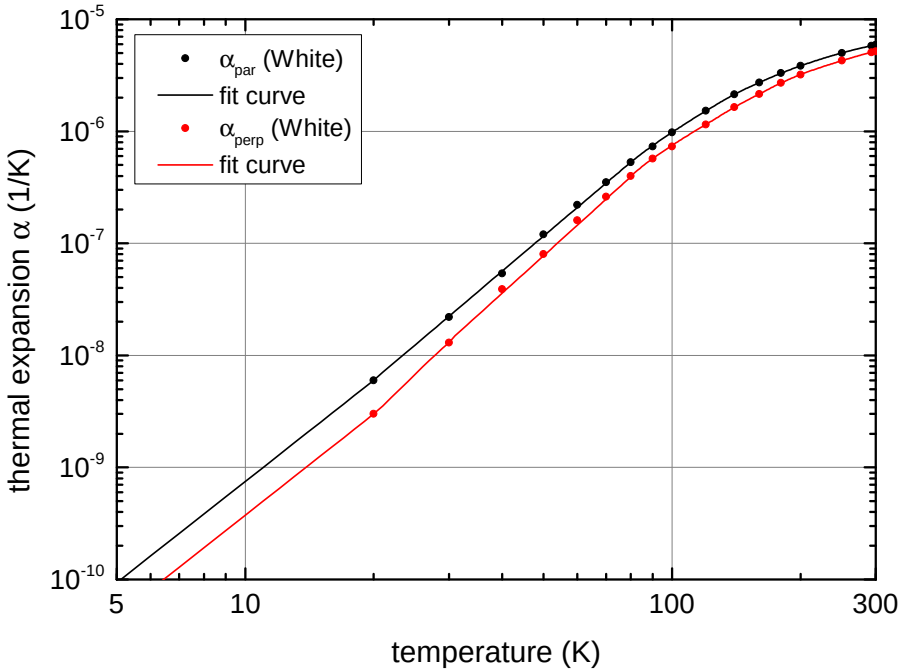

Experimental values have been taken from White [21]. The directions $\alpha_{\parallel}$ and $\alpha_{\perp}$ are given with respect to the three-fold axis in sapphire.

Specific heat

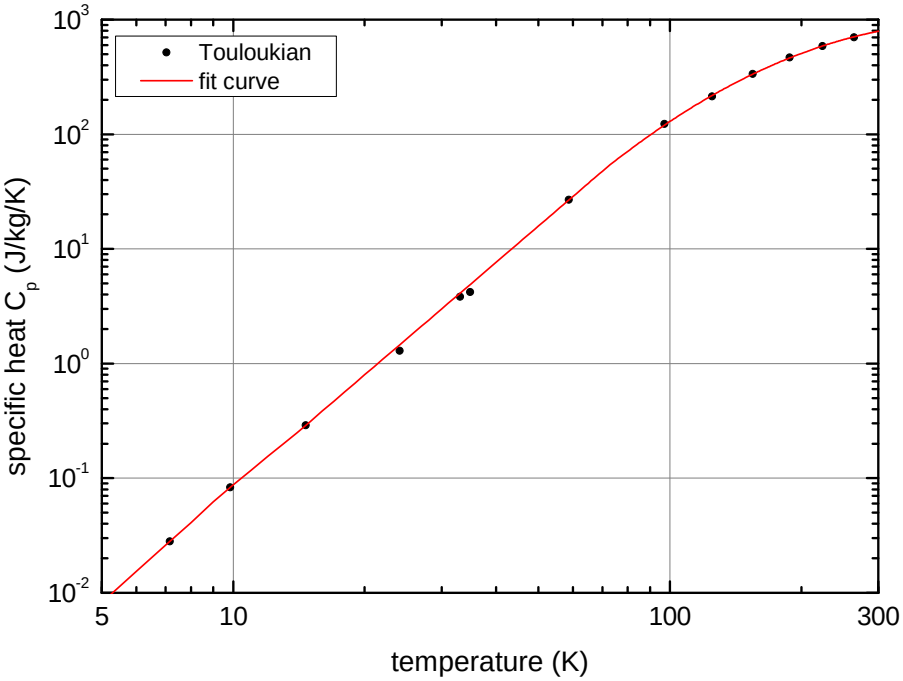

Experimental values have been taken from Touloukian [5].

Thermal conductivity

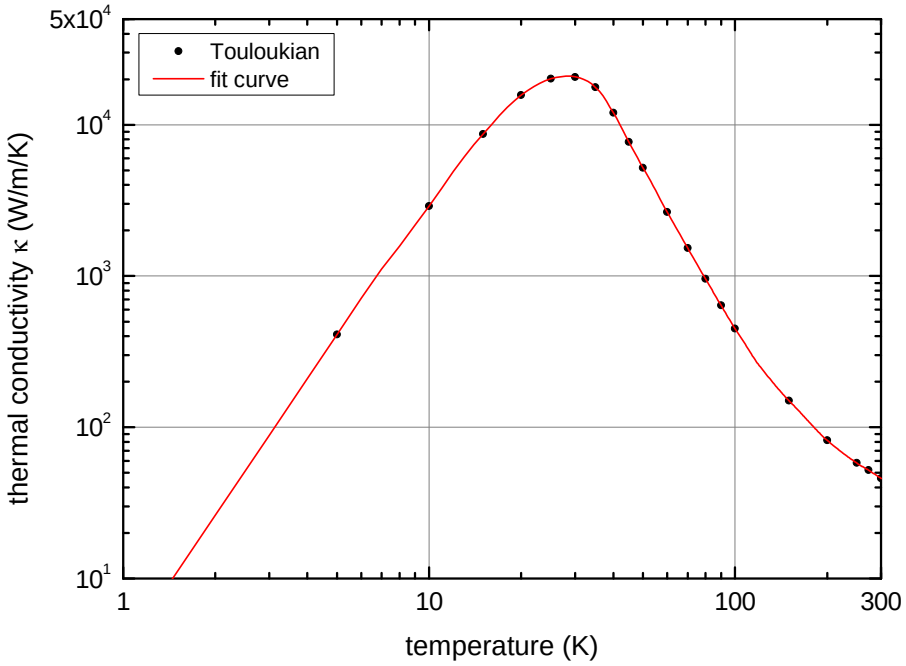

Experimental values have been taken from Touloukian [5]. The fit curve follows the experimental data for large and pure samples. As in such samples the influence of the surface and defects is minimized the presented curve serves as an upper bound on sapphire. Although the sapphire structure allows for an anisotropic behavior of thermal conductivity no differences are discussed in the literature.

Thermo-optic coefficient

In the literature there exist a few publications reporting on the temperature dependent refractive index (e. g. Ref. [22, 23]). Typically they refer to a direct measurement of the refractive index and obtain a value for beta by a numerical derivation of a fit to the measured data. Due to the small changes of n at low temperatures the inaccuracy of this analysis scheme becomes significant especially at low temperatures below $\sim 100\,\mathrm{K}$. Further results for a wavelength at 1064 nm are quite rare, while mainly the visible spectral range has been investigated. For this reason we do not present a fit to the thermo-optic parameter of sapphire. Instead for the use in a gravitational wave detector at 1064 nm the most valuable number is reported by Tomaru et al. [24]. For temperatures below 40 K they give an upper bound on β of $9 \times 10^{-8}\,\mathrm{K}^{-1}$.

Data set

An excerpt of the numerical data is given in the following table. Extrapolations in the low temperature regime have been performed assuming a T^3 law.

T (K)	$\alpha_\parallel$ (K^{-1})	$\alpha_\perp$ (K^{-1})	C_p ($J\,kg^{-1}\,K^{-1}$)	κ ($W\,m^{-1}\,K^{-1}$)
1	7.50×10^{-13}	3.75×10^{-13}	6.57×10^{-5}	3.28
2	6.00×10^{-12}	3.00×10^{-12}	5.25×10^{-4}	2.62×10^{1}
3	2.03×10^{-11}	1.01×10^{-11}	1.77×10^{-3}	8.86×10^{1}
4	4.80×10^{-11}	2.40×10^{-11}	4.20×10^{-3}	2.10×10^{2}
5	9.38×10^{-11}	4.69×10^{-11}	8.21×10^{-3}	4.10×10^{2}
6	1.62×10^{-10}	8.10×10^{-11}	1.54×10^{-2}	7.14×10^{2}
7	2.57×10^{-10}	1.29×10^{-10}	2.61×10^{-2}	1.11×10^{3}
8	3.84×10^{-10}	1.92×10^{-10}	4.10×10^{-2}	1.58×10^{3}
9	5.47×10^{-10}	2.73×10^{-10}	6.20×10^{-2}	2.17×10^{3}
10	7.50×10^{-10}	3.75×10^{-10}	8.74×10^{-2}	2.90×10^{3}
12	1.30×10^{-9}	6.48×10^{-10}	1.55×10^{-1}	4.91×10^{3}
14	2.06×10^{-9}	1.03×10^{-9}	2.49×10^{-1}	7.41×10^{3}
16	3.07×10^{-9}	1.54×10^{-9}	3.85×10^{-1}	1.01×10^{4}
18	4.37×10^{-9}	2.19×10^{-9}	5.66×10^{-1}	1.31×10^{4}
20	6.00×10^{-9}	3.00×10^{-9}	7.98×10^{-1}	1.57×10^{4}
22	8.21×10^{-9}	4.20×10^{-9}	1.09	1.79×10^{4}
24	1.09×10^{-8}	5.84×10^{-9}	1.45	1.95×10^{4}
26	1.41×10^{-8}	7.87×10^{-9}	1.88	2.06×10^{4}
28	1.79×10^{-8}	1.03×10^{-8}	2.39	2.10×10^{4}
30	2.23×10^{-8}	1.30×10^{-8}	2.99	2.08×10^{4}
32	2.75×10^{-8}	1.66×10^{-8}	3.69	2.00×10^{4}
34	3.35×10^{-8}	2.05×10^{-8}	4.50	1.86×10^{4}
36	4.02×10^{-8}	2.50×10^{-8}	5.42	1.67×10^{4}
38	4.79×10^{-8}	3.01×10^{-8}	6.47	1.43×10^{4}
40	5.65×10^{-8}	3.59×10^{-8}	7.65	1.20×10^{4}
45	8.27×10^{-8}	5.39×10^{-8}	1.12×10^{1}	7.70×10^{3}
50	1.16×10^{-7}	7.76×10^{-8}	1.58×10^{1}	5.20×10^{3}
55	1.58×10^{-7}	1.08×10^{-7}	2.16×10^{1}	3.68×10^{3}
60	2.09×10^{-7}	1.45×10^{-7}	2.87×10^{1}	2.65×10^{3}
65	2.71×10^{-7}	1.92×10^{-7}	3.74×10^{1}	1.99×10^{3}
70	3.44×10^{-7}	2.48×10^{-7}	4.76×10^{1}	1.53×10^{3}
75	4.30×10^{-7}	3.14×10^{-7}	5.89×10^{1}	1.20×10^{3}
80	5.30×10^{-7}	4.00×10^{-7}	7.08×10^{1}	9.60×10^{2}
85	6.34×10^{-7}	4.84×10^{-7}	8.40×10^{1}	7.79×10^{2}
90	7.44×10^{-7}	5.69×10^{-7}	9.82×10^{1}	6.40×10^{2}
95	8.60×10^{-7}	6.58×10^{-7}	1.13×10^{2}	5.32×10^{2}
100	9.80×10^{-7}	7.50×10^{-7}	1.29×10^{2}	4.50×10^{2}

T (K)	$\alpha_{\parallel}$ (K^{-1})	$\alpha_{\perp}$ (K^{-1})	C_p ($\mathrm{J\,kg^{-1}\,K^{-1}}$)	κ ($\mathrm{W\,m^{-1}\,K^{-1}}$)
110	1.24×10^{-6}	9.42×10^{-7}	1.63×10^{2}	3.34×10^{2}
120	1.52×10^{-6}	1.15×10^{-6}	2.00×10^{2}	2.56×10^{2}
130	1.83×10^{-6}	1.39×10^{-6}	2.37×10^{2}	2.09×10^{2}
140	2.14×10^{-6}	1.64×10^{-6}	2.76×10^{2}	1.75×10^{2}
150	2.43×10^{-6}	1.89×10^{-6}	3.16×10^{2}	1.50×10^{2}
160	2.72×10^{-6}	2.15×10^{-6}	3.55×10^{2}	1.31×10^{2}
170	3.01×10^{-6}	2.43×10^{-6}	3.94×10^{2}	1.15×10^{2}
180	3.30×10^{-6}	2.70×10^{-6}	4.33×10^{2}	1.01×10^{2}
190	3.58×10^{-6}	2.96×10^{-6}	4.71×10^{2}	9.04×10^{1}
200	3.84×10^{-6}	3.21×10^{-6}	5.07×10^{2}	8.20×10^{1}
210	4.09×10^{-6}	3.44×10^{-6}	5.43×10^{2}	7.55×10^{1}
220	4.34×10^{-6}	3.66×10^{-6}	5.77×10^{2}	7.00×10^{1}
230	4.57×10^{-6}	3.87×10^{-6}	6.09×10^{2}	6.54×10^{1}
240	4.80×10^{-6}	4.07×10^{-6}	6.40×10^{2}	6.14×10^{1}
250	5.01×10^{-6}	4.27×10^{-6}	6.70×10^{2}	5.80×10^{1}
260	5.21×10^{-6}	4.47×10^{-6}	6.98×10^{2}	5.52×10^{1}
270	5.40×10^{-6}	4.66×10^{-6}	7.24×10^{2}	5.28×10^{1}
280	5.59×10^{-6}	4.85×10^{-6}	7.48×10^{2}	5.04×10^{1}
290	5.75×10^{-6}	5.02×10^{-6}	7.71×10^{2}	4.81×10^{1}
300	5.90×10^{-6}	5.15×10^{-6}	7.92×10^{2}	4.60×10^{1}

3.3 Silicon

Silicon crystallizes in the diamond structure belonging to the cubic crystal system. The growth of silicon crystals is mainly along a {111} or a {100} plane [25]. This is due to the fact that the {111} plane shows the highest atom density. Nevertheless for completeness also the {110} orientation will be considered. The orientation of these planes in the lattice is presented in Fig. 3.2

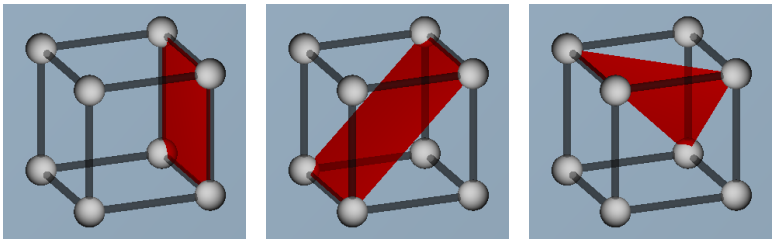

(a) (100) (b) (110) (c) (111)

Figure 3.2: Visualization of typical crystallographic planes in silicon.

3.3.1 Elastic properties

Condensating in the cubic crystal system silicon possesses three independent elastic constants. The structure of the stiffness matrix reads

$$\hat{C}_{ij} = \begin{pmatrix} c_{11} & c_{12} & c_{12} & 0 & 0 & 0 \\ & c_{11} & c_{12} & 0 & 0 & 0 \\ & & c_{11} & 0 & 0 & 0 \\ & & & c_{44} & 0 & 0 \\ & & & & c_{44} & 0 \\ & & & & & c_{44} \end{pmatrix} . \tag{3.15}$$

For a temperature of 20 °C McSkimin [15] reports the following coefficients

$$c_{11} = 165.7\,\mathrm{GPa}, \qquad c_{12} = 63.9\,\mathrm{GPa}, \qquad c_{44} = 79.6\,\mathrm{GPa}. \tag{3.16}$$

McSkimin further investigated the temperature dependence of the elastic constants in silicon. Down to 70 K all components show a relative change below 2%. Again in most considerations this weak temperature dependence can be neglected. The density of silicon reads

$$\rho = 2330\,\mathrm{kg\,m^{-3}} . \tag{3.17}$$

Under an uniaxial load (as for e. g. in flexural modes of beams) the elastic behavior can be modelled as isotropic. Then an effective Young's modulus and Poisson ratio can be defined which are dependend on the crystalline orientation of the beam axis. This approach presented by Wortman and Evans [26] shows effective Young's moduli in a range from 130 GPa to 189 GPa.

For more difficult geometries or other load cases a more rigorous approach becomes necessary. This is also true for a thermal noise estimate using the Fluctuation-Dissipation-Theorem for an interferometer component. Then the full anisotropic structure of silicon has to be taken into account. In typical finite element codes one can thus orient the geometry axis within the coordinates of the elastic tensor. The other way presented here is to transform the elastic tensor to new coordinates and present the new component values. Table 3.3.1 illustrates the results of this process. In the shape of the new elastic tensor components the symmetry of the respective orientation becomes visible. Previously this approach has been discussed by Hopcroft et al. [27].

Table 3.5: Elasticity tensor for silicon along different crystallographic axes. The presented components are valid for a coordinate system whose z-axis is oriented along the stated crystal direction. The Voigt notation $\hat{C}_{ij}$ is used to show the components of the elasticity tensor. All presented values are valid for a temperature of 20 °C and taken from [15].

orientation symmetry	[110] tetragonal	[111] trigonal
A_{ij}	$\begin{pmatrix} \frac{\sqrt{2}}{2} & -\frac{\sqrt{2}}{2} & 0 \\ \frac{\sqrt{2}}{2} & \frac{\sqrt{2}}{2} & 0 \\ 0 & 0 & 1 \end{pmatrix}$	$\frac{1}{\sqrt{6}} \begin{pmatrix} \sqrt{3} & 0 & -\sqrt{3} \\ -1 & 2 & -1 \\ \sqrt{2} & \sqrt{2} & \sqrt{2} \end{pmatrix}$
$\hat{C}_{ij}$	$\begin{pmatrix} d_{11} & d_{12} & d_{13} & 0 & 0 & 0 \\ & d_{11} & d_{13} & 0 & 0 & 0 \\ & & d_{33} & 0 & 0 & 0 \\ & & & d_{44} & 0 & 0 \\ & & & & d_{44} & 0 \\ & & & & & d_{66} \end{pmatrix}$	$\begin{pmatrix} e_{11} & e_{12} & e_{13} & e_{14} & 0 & 0 \\ & e_{11} & e_{13} & -e_{14} & 0 & 0 \\ & & e_{33} & 0 & 0 & 0 \\ & & & e_{44} & 0 & 0 \\ & & & & e_{44} & e_{14} \\ & & & & & e_{66} \end{pmatrix}$
	$d_{11} = 194.4\,\mathrm{GPa}$ $d_{12} = 35.2\,\mathrm{GPa}$ $d_{33} = 165.7\,\mathrm{GPa}$ $d_{13} = 63.9\,\mathrm{GPa}$ $d_{44} = 79.6\,\mathrm{GPa}$ $d_{66} = 50.9\,\mathrm{GPa}$	$e_{11} = 194.4\,\mathrm{GPa}$ $e_{12} = 54.4\,\mathrm{GPa}$ $e_{33} = 203.9\,\mathrm{GPa}$ $e_{13} = 44.8\,\mathrm{GPa}$ $e_{14} = 13.5\,\mathrm{GPa}$ $e_{44} = 60.5\,\mathrm{GPa}$ $e_{66} = \frac{1}{2}(e_{11} - e_{12})$ $= 70.0\,\mathrm{GPa}$

3.3.2 Thermal properties

Thermal expansion

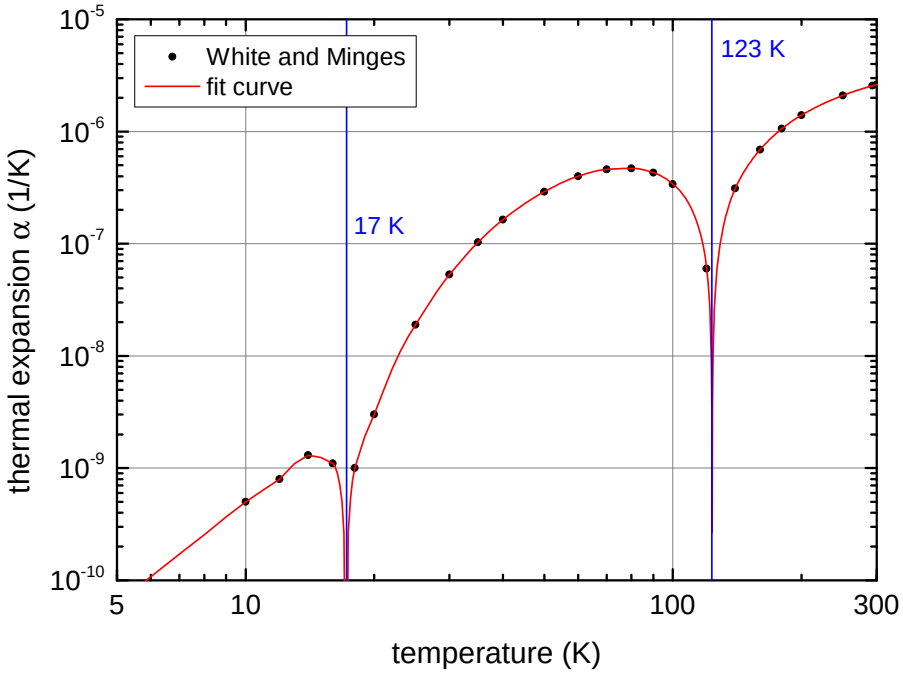

Experimental values have been taken from White and Minges [10]. Note that α is negative between 17 K and 123 K.

Thermo-optic coefficient

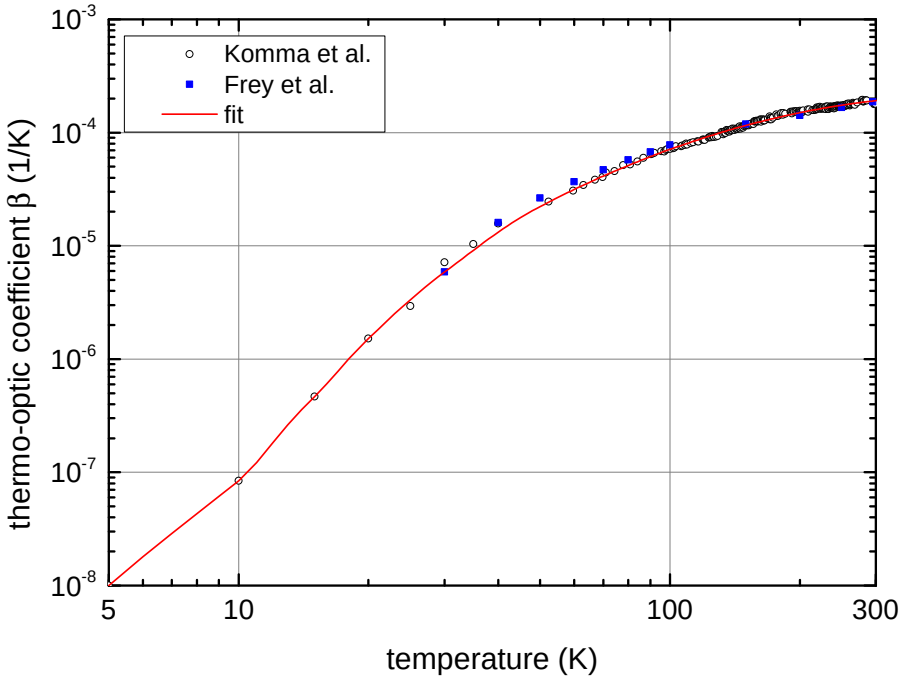

Experimental values have been taken from Komma et al. [28] and from Frey and Leviton [29].

Specific heat

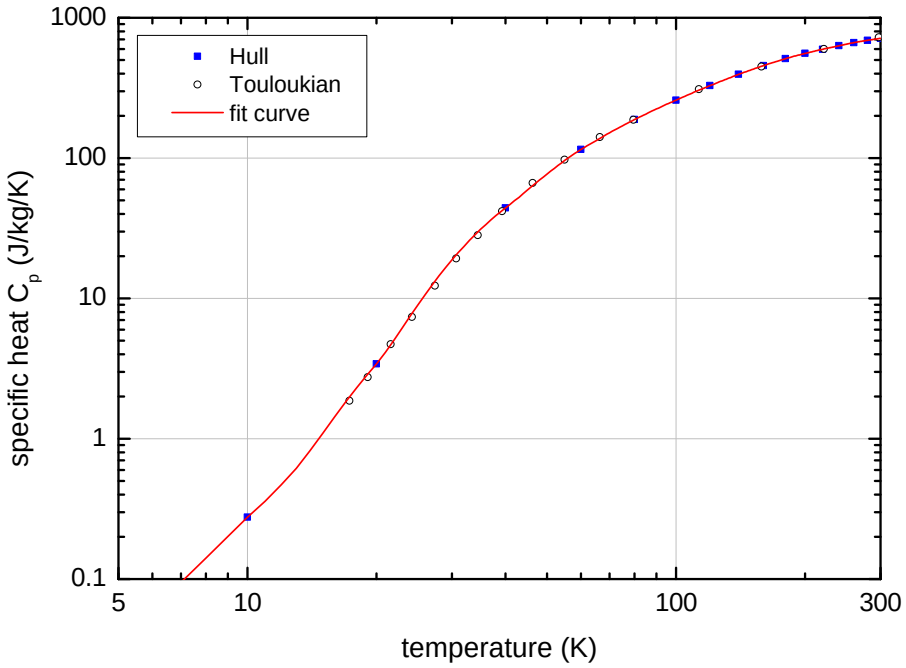

Experimental values have been taken from Hull [30] and from Touloukian [5].

Thermal conductivity

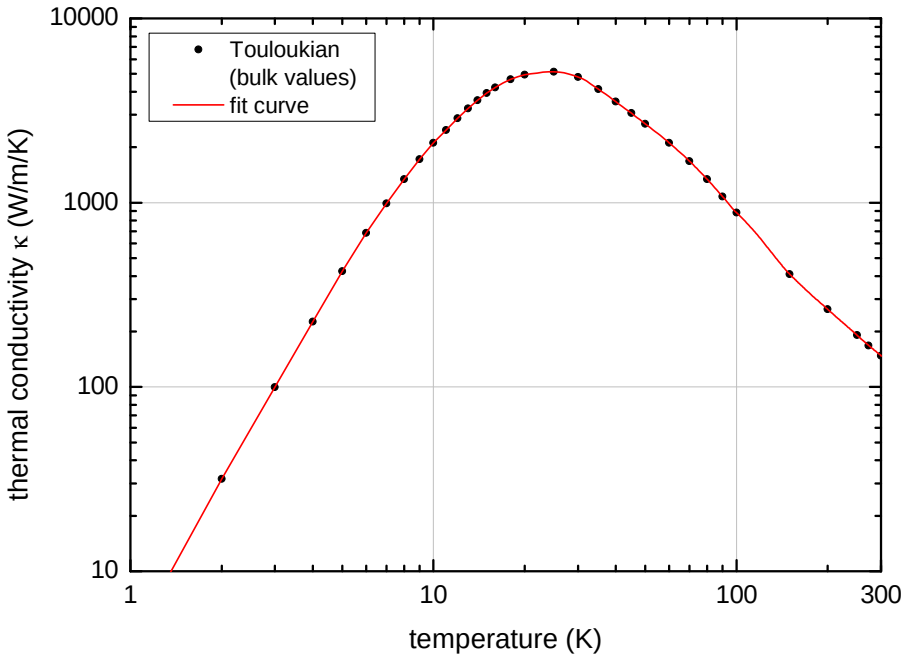

Experimental values have been taken from Touloukian [5]. The fit curve follows the experimental data for large and pure samples. As in such samples the influence of the surface and defects is minimized the presented curve serves as an upper bound on silicon.

Data set

An excerpt of the numerical data is given in the following table. Extrapolations in the low temperature regime have been performed assuming a T^3 law.

T (K)	α (K^{-1})	β (K^{-1})	C_p ($J\,kg^{-1}\,K^{-1}$)	κ ($W\,m^{-1}\,K^{-1}$)
1	5.00×10^{-13}	8.00×10^{-11}	2.76×10^{-4}	3.96
2	4.00×10^{-12}	6.40×10^{-10}	2.21×10^{-3}	3.17×10^{1}
3	1.35×10^{-11}	2.16×10^{-9}	7.45×10^{-3}	9.98×10^{1}
4	3.20×10^{-11}	5.12×10^{-9}	1.77×10^{-2}	2.26×10^{2}
5	6.34×10^{-11}	1.00×10^{-8}	3.45×10^{-2}	4.24×10^{2}
6	1.08×10^{-10}	1.80×10^{-8}	5.96×10^{-2}	6.86×10^{2}
7	1.72×10^{-10}	2.89×10^{-8}	9.47×10^{-2}	9.91×10^{2}
8	2.56×10^{-10}	4.33×10^{-8}	1.41×10^{-1}	1.34×10^{3}
9	3.67×10^{-10}	6.15×10^{-8}	2.01×10^{-1}	1.72×10^{3}
10	5.00×10^{-10}	8.40×10^{-8}	2.76×10^{-1}	2.11×10^{3}
12	8.00×10^{-10}	1.82×10^{-7}	4.70×10^{-1}	2.87×10^{3}
14	1.30×10^{-9}	3.58×10^{-7}	8.22×10^{-1}	3.60×10^{3}
16	1.10×10^{-9}	6.02×10^{-7}	1.44	4.22×10^{3}
17	2.60×10^{-10}	7.84×10^{-7}	1.85	4.47×10^{3}
18	-1.00×10^{-9}	1.00×10^{-6}	2.31	4.67×10^{3}
19	-1.90×10^{-9}	1.25×10^{-6}	2.84	4.83×10^{3}
20	-3.00×10^{-9}	1.52×10^{-6}	3.41	4.94×10^{3}
22	-7.56×10^{-9}	2.14×10^{-6}	5.05	5.06×10^{3}
24	-1.48×10^{-8}	2.91×10^{-6}	7.52	5.13×10^{3}
26	-2.40×10^{-8}	3.80×10^{-6}	1.07×10^{1}	5.12×10^{3}
28	-3.73×10^{-8}	4.79×10^{-6}	1.45×10^{1}	4.99×10^{3}
30	-5.30×10^{-8}	5.86×10^{-6}	1.88×10^{1}	4.81×10^{3}
32	-7.12×10^{-8}	7.05×10^{-6}	2.35×10^{1}	4.57×10^{3}
34	-9.21×10^{-8}	8.41×10^{-6}	2.85×10^{1}	4.27×10^{3}
36	-1.14×10^{-7}	9.91×10^{-6}	3.36×10^{1}	4.00×10^{3}
38	-1.39×10^{-7}	1.15×10^{-5}	3.89×10^{1}	3.76×10^{3}
40	-1.64×10^{-7}	1.32×10^{-5}	4.41×10^{1}	3.53×10^{3}
45	-2.28×10^{-7}	1.77×10^{-5}	5.91×10^{1}	3.06×10^{3}
50	-2.90×10^{-7}	2.23×10^{-5}	7.70×10^{1}	2.68×10^{3}
55	-3.50×10^{-7}	2.68×10^{-5}	9.62×10^{1}	2.37×10^{3}
60	-4.00×10^{-7}	3.15×10^{-5}	1.15×10^{2}	2.11×10^{3}
65	-4.38×10^{-7}	3.64×10^{-5}	1.33×10^{2}	1.88×10^{3}
70	-4.60×10^{-7}	4.13×10^{-5}	1.52×10^{2}	1.68×10^{3}
75	-4.67×10^{-7}	4.62×10^{-5}	1.70×10^{2}	1.50×10^{3}
80	-4.70×10^{-7}	5.12×10^{-5}	1.88×10^{2}	1.34×10^{3}
85	-4.57×10^{-7}	5.62×10^{-5}	2.06×10^{2}	1.20×10^{3}
90	-4.30×10^{-7}	6.13×10^{-5}	2.24×10^{2}	1.08×10^{3}
95	-3.91×10^{-7}	6.63×10^{-5}	2.41×10^{2}	9.71×10^{2}

T (K)	α (K^{-1})	β (K^{-1})	C_p ($\mathrm{J\,kg^{-1}\,K^{-1}}$)	κ ($\mathrm{W\,m^{-1}\,K^{-1}}$)
100	-3.40×10^{-7}	7.11×10^{-5}	2.59×10^{2}	8.84×10^{2}
110	-2.13×10^{-7}	8.06×10^{-5}	2.94×10^{2}	7.53×10^{2}
120	-6.00×10^{-8}	9.00×10^{-5}	3.28×10^{2}	6.38×10^{2}
130	1.18×10^{-7}	9.90×10^{-5}	3.62×10^{2}	5.42×10^{2}
140	3.10×10^{-7}	1.08×10^{-4}	3.95×10^{2}	4.65×10^{2}
150	5.00×10^{-7}	1.16×10^{-4}	4.26×10^{2}	4.09×10^{2}
160	6.90×10^{-7}	1.23×10^{-4}	4.56×10^{2}	3.69×10^{2}
170	8.78×10^{-7}	1.31×10^{-4}	4.85×10^{2}	3.35×10^{2}
180	1.06×10^{-6}	1.38×10^{-4}	5.11×10^{2}	3.08×10^{2}
190	1.24×10^{-6}	1.44×10^{-4}	5.35×10^{2}	2.84×10^{2}
200	1.40×10^{-6}	1.50×10^{-4}	5.57×10^{2}	2.64×10^{2}
210	1.55×10^{-6}	1.56×10^{-4}	5.78×10^{2}	2.46×10^{2}
220	1.70×10^{-6}	1.61×10^{-4}	5.97×10^{2}	2.30×10^{2}
230	1.84×10^{-6}	1.66×10^{-4}	6.15×10^{2}	2.16×10^{2}
240	1.98×10^{-6}	1.70×10^{-4}	6.32×10^{2}	2.03×10^{2}
250	2.10×10^{-6}	1.75×10^{-4}	6.49×10^{2}	1.91×10^{2}
260	2.22×10^{-6}	1.79×10^{-4}	6.65×10^{2}	1.80×10^{2}
270	2.33×10^{-6}	1.82×10^{-4}	6.79×10^{2}	1.71×10^{2}
280	2.43×10^{-6}	1.86×10^{-4}	6.91×10^{2}	1.62×10^{2}
290	2.53×10^{-6}	1.89×10^{-4}	7.03×10^{2}	1.55×10^{2}
300	2.62×10^{-6}	1.91×10^{-4}	7.13×10^{2}	1.48×10^{2}

Bibliography

[1] N. W. Ashcroft and N. D. Mermin. *Solid state physics*. Cengage Learning EMEA, 2000.

[2] C. Kittel. *Introduction to Solid State Physics*. Wiley&Sons, 1995.

[3] F. Reif. *Fundamentals of Statistical and Thermal Physics*. McGraw-Hill, 1985.

[4] C. Enss and S. Hunklinger. *Low-Temperature Physics*. Springer-Verlag Berlin Heidelberg, 2005.

[5] Y. S. Touloukian. *Thermophysical properties of matter*. IFI/Plenum, New York-Washington, 1970.

[6] T. Ruf, R. W. Henn, M. Asen-Palmer, E. Gmelin, M. Cardona, H.-J. Pohl, G. G. Devyatych, and P. G. Sennikov. Thermal conductivity of isotopically enriched silicon. *Solid State Communications*, 115:243–247, 2000.

[7] M. Asheghi, K. Kurabayashi, R. Kasnavi, and K. E. Goodson. Thermal conduction in doped single-crystal silicon films. *Journal of Applied Physics*, 91(8):5079–5088, 2002.

[8] P. D. Thacher. Effect of Boundaries and Isotopes on the Thermal Conductivity of LiF. *Phys. Rev.*, 156(3):975–988, 1967.

[9] R. C. Zeller and R. O. Pohl. Thermal Conductivity and Specific Heat of Noncrystalline Solids. *Phys. Rev. B*, 4(6):2029–2041, 1971.

[10] G. K. White. Thermal expansion of reference materials: copper, silica and silicon. *J. Phys. D*, 6:2070–2078, 1973.

[11] M. Fox. *Optical Properties of Solids*. Oxford University Press, 2010.

[12] L. D. Landau and E. M. Lifshitz. *Theory of Elasticity*. Pergamon Press, New York, 1986.

[13] J. F. Nye. *Physical Properties of Crystals*. Oxford University Press, 1985.

[14] www.comsol.com.

[15] H. J. McSkimin. Measurement of Elastic Constants at Low Temperatures by Means of Ultrasonic Waves–Data for Silicon and Germanium Single Crystals, and for Fused Silica. *Journal of Applied Physics*, 24(8):988–997, 1953.

[16] D. B. Leviton and B. J. Frey. Temperature-dependent absolute refractive index measurements of synthetic fused silica. arXiv:0805.0091v1 [physics.optics], 2008.

[17] H. Bialas and H. J. Stolz. Lattice Dynamics of Sapphire (Corundum). *Z. Physik B*, 21:319–324, 1975.

[18] C. P. Khattak and F. Schmid. Growth of the world's largest sapphire crystals. *Journal of Crystal Growth*, 225(2-4):572 – 579, 2001.

[19] W. E. Tefft. Elastic Constants of Synthetic Single Crystal Corundum. *JOURNAL OF RESEARCH of the National Bureau of Standards–A. Physics and Chemistry*, 70A(4):277–280, 1966.

[20] B. T. Bernstein. Elastic Constants of Synthetic Sapphire at 27 °C. *Journal of Applied Physics*, 34(1):169–172, 1963.

[21] G. K. White. Reference materials for thermal expansion: certified or not? *Thermochimica Acta*, 218:83–99, 1993.

[22] J. Tapping and M. L. Reilly. Index of refraction of sapphire between 24 and 1060 °C for wavelengths of 633 and 799 nm. *J. Opt. Soc. Am. A*, 3(5):610–616, 1986.

[23] A. C. DeFranzo and B. G. Pazol. Index of refraction measurement on sapphire at low temperatures and visible wavelengths. *Appl. Opt.*, 32(13):2224–2234, 1993.

[24] T. Tomaru, T. Suzuki, S. Miyoki, T. Uchiyama, C. T. Taylor, A. Yamamoto, T. Shintomi, M. Ohashi, and K. Kuroda. Thermal lensing in an cryogenic sapphire substrates. *Classical and Quantum Gravity*, 19:2045–2049, 2002.

[25] K. E. Bean and P. S. Gleim. The Influence of Crystal Orientation on Silicon Semiconductor Processing. *Proceedings of the IEEE*, 57(9):1469–1476, 1969.

[26] J. J. Wortman and R. A. Evans. Young's Modulus, Shear Modulus and Poisson's Ratio in Silicon and Germanium. *J. Appl. Phys.*, 36(1):153–156, 1965.

[27] M. A. Hopcroft, W. D. Nix, and T. W. Kenny. What is the Young's Modulus of Silicon? *J. Microelectromech. Syst.*, 19(2):229–238, 2010.

[28] J. Komma, C. Schwarz, G. Hofmann, D. Heinert, and R. Nawrodt. Thermo-optic coefficient of silicon at 1550 nm and cryogenic temperatures. *Appl. Phys. Lett.*, 101:041905, 2012.

[29] B. J. Frey and D. B. Leviton. Temperature-dependent refractive index of silicon and germanium. arXiv:physics/0606168v1 [physics.optics], 2006.

[30] R. Hull, editor. *Properties of Crystalline Silicon*. INSPEC, the Institution of Electrical Engineers, London, UK, 1999.